Fluctuation effects in rotating Bose-Einstein condensates with broken SU(2) and U(1) × U(1) symmetries in the presence of intercomponent density-density interactions

Peder Notto Galteland,[1] Egor Babaev,[2] and Asle Sudbø[1]
[1]*Department of Physics, Norwegian University of Science and Technology, N-7491 Trondheim, Norway*
[2]*Department of Theoretical Physics, The Royal Institute of Technology, 10691 Stockholm, Sweden*
(Received 16 October 2014; published 6 January 2015)

Thermal fluctuations and melting transitions for rotating single-component superfluids have been intensively studied and are well understood. In contrast, the thermal effects on vortex states for two-component superfluids with density-density interaction, which have a much richer variety of vortex ground states, have been much less studied. Here, we investigate the thermal effects on vortex matter in superfluids with U(1) × U(1) broken symmetries and intercomponent density-density interactions, as well as the case with a larger SU(2) broken symmetry obtainable from the [U(1) × U(1)]-symmetric case by tuning scattering lengths. In the former case we find that, in addition to first-order melting transitions, the system exhibits thermally driven phase transitions between square and hexagonal lattices. Our main result, however, concerns the case where the condensate exhibits SU(2) symmetry, and where vortices are not topological. At finite temperature, the system exhibits effects which do not have a counterpart in single-component systems. Namely, it has a state where thermally averaged quantities show no regular vortex lattice, yet the system retains superfluid coherence along the axis of rotation. In such a state, the thermal fluctuations result in transitions between different (nearly) degenerate vortex states without undergoing a melting transition. Our results apply to multicomponent Bose-Einstein condensates, and we suggest how to detect some of these unusual effects experimentally in such systems.

DOI: 10.1103/PhysRevA.91.013605 PACS number(s): 67.85.Fg, 67.25.dk, 67.60.Bc, 67.85.Jk

I. INTRODUCTION

Bose-Einstein condensates (BECs) with a multicomponent order parameter, and the topological defects such systems support, represent a topic of great current interest in condensed matter physics [1–15]. Such multicomponent condensates may be realized as mixtures of different atoms, mixtures of different isotopes of an atom, or mixtures of different hyperfine spin states of an atom. The interest in such condensates from a fundamental physics point of view is mainly attributed to the fact that one may tune various interaction parameters over a wide range in a BEC. This enables the study of a variety of physical effects which are not easily observed in other superfluid systems such as ^{3}He and ^{4}He.

The behavior of a single-component BEC under rotation is well known. The ground state is a hexagonal lattice of vortex defects which melts to a vortex liquid via a first-order phase transition. This is well described by the London model, where amplitude fluctuations may be ignored. Over the years, in the context of studying vortex lattice melting in high-T_c superconductors, many works have confirmed this through numerical Monte Carlo simulations for systems in the frozen gauge, three-dimensional (3D) *XY*, and Villain approximations [16–25], as well as in the lowest-Landau-level approximation [26], and by mapping it to a model of 2D bosons [27]. Single-component condensates have been available experimentally for quite some time [28,29], and the hexagonal lattice ground state has been verified [30].

Condensates with two components of the order parameter have also been studied extensively. Analytical works focusing on determining the $T = 0$ ground states have demonstrated a range of interesting possible lattice structures [5,6,10,13,14,31]. By varying the ratio between inter- and intracomponent couplings, the ground-state lattice undergoes a structural change from hexagonal symmetry through square symmetry to double-core lattices and interwoven sheets of vortices. Similar systems with three components have also been studied [15]. Experimentally, spinor condensates have been realized in two general classes of systems. The first option is to use one species of atoms, usually rubidium, and prepare it in two separate hyperfine spin states [1,2]. Vortices [3] and vortex lattices [7] have been realized in these binary mixtures, where both hexagonal and square vortex lattice states were observed. The other option is to mix condensates of two different species of atoms [4,12]. The use of Feshbach resonances [32,33] allows direct tuning of the scattering lengths, and by extension the inter- and intracomponent interactions of multicomponent condensates [8,9,11].

In this paper, we consider a specific model of a two-component BEC, which has the full range of fluctuations of the order-parameter field included, as well as intercomponent density-density interactions. We consider the model with U(1) × U(1) and as SU(2) symmetries. For the U(1) × U(1) case, we find a succession of square and hexagonal vortex ground-state patterns as the intercomponent interaction strength is varied, along with the possibility of thermal reconstruction from a square to a hexagonal vortex lattice as temperature is reduced.

The SU(2)-symmetric case is interesting and experimentally realizable. In this case U(1) vortices are no longer topological, in contrast to the [U(1) × U(1)]-symmetric case. In this case, when fluctuation effects are included we find a highly unusual vortex state where there is no sign of any vortex lattice. Nonetheless, global phase coherence persists. This state of vortex matter is a direct consequence of massless amplitude fluctuations in the order parameter, when the broken symmetry of the system is SU(2). At the SU(2) point, but at lower temperatures, we also observe dimerized vortex ground-state patterns.

The paper is organized as follows. The model and definitions of relevant quantities are presented in Sec. II. The technical details of the Monte Carlo simulations are briefly considered in Sec. III. In Sec. IV, the results are presented and discussed. In Sec. V, we discuss how to experimentally verify the results we find. Some technical details and the investigation of the order of the melting transitions with full amplitude distributions included, for the cases $N = 1$ and $N = 2$, are relegated to Appendixes.

II. MODEL AND DEFINITIONS

In this section we present the model used in the paper, first in a continuum description and then on a three-dimensional cubic lattice appropriate for Monte Carlo simulations. The relevant quantities for the discussion are also defined.

A. Continuum model

We consider a general Ginzburg-Landau (GL) model of an N-component Bose-Einstein condensate, coupled to a uniform external field, which in the thermodynamical limit is defined as

$$\mathcal{Z} = \int \prod_i^N \mathcal{D}\psi_i' e^{-\beta H}, \tag{1}$$

where

$$H = \int d^3r \left[\sum_{i=1}^{N} \sum_{\mu=1}^{3} \frac{\hbar^2}{2m_i} \left| \left(\partial_\mu - i \frac{2\pi}{\Phi_0} A_\mu' \right) \psi_i' \right|^2 + \sum_i^N \alpha_i' |\psi_i'|^2 + \sum_{i,j=1}^{N} g_{ij}' |\psi_i'|^2 |\psi_j'|^2 \right] \tag{2}$$

is the Hamiltonian. Here, the field A_μ' formally appears as a nonfluctuating gauge field and parametrizes the angular velocity of the system. The fields ψ_i' are dimensionful complex fields, i and j are indices running from 1 to N denoting the component of the order parameter (a "color" index), α_i' and g_{ij}' are Ginzburg-Landau parameters, Φ_0 is the coupling constant to the rotation induced vector potential, and m_i is the particle mass of species i. For mixtures consisting of different atoms or different isotopes of one atom, the masses will depend on the index i, while for mixtures consisting of atoms in different hyperfine spin states, the masses are independent of i. The inter- and intracomponent coupling parameters g_{ij}' are related to real inter- and intracomponent scattering lengths a_{ij} in the following way:

$$g_{ii}' = \frac{4\pi\hbar^2 a_{ii}}{m_i}, \tag{3}$$

$$g_{ij}' = \frac{8\pi\hbar^2 a_{ij}}{m_{ij}} \quad (i \neq j), \tag{4}$$

where $m_{ij} = m_i m_j/(m_i + m_j)$ is the reduced mass. In this paper we focus on using BECs of homonuclear gases with several components in different hyperfine states; hence $m_i = m \; \forall \, i$. Intercomponent drag in BEC mixtures has been considered in previous works using Monte Carlo simulation (ignoring amplitude fluctuations), but we will not consider this case here [34–38].

We find it convenient for our purposes to rewrite (2) in the following form, the details of which are relegated to Appendix A:

$$H = \int d^3r \left[\frac{1}{2} (D_\mu \Psi)^\dagger (D_\mu \Psi) + V(\Psi) \right]. \tag{5}$$

Here, Ψ is an N-component spinor of dimensionless complex fields, which consists of an amplitude and a phase, $\psi_i = |\psi_i| \exp(i\theta_i)$, $D_\mu = \partial_\mu - i \frac{2\pi}{\Phi_0} A_\mu'$ is the covariant derivative, and summation over repeated spatial indices is implied. We neglect, for simplicity, the presence of a trap and the centrifugal part of the potential. We consider only the case where the vector potential is applied to each component of Ψ, as follows from the fact that the masses are independent of species index i.

We have studied this model in detail with $N = 2$, where we write the potential in the form

$$V(\Psi) = \eta(|\Psi|^2 - 1)^2 + \omega(\Psi^\dagger \sigma_z \Psi)^2. \tag{6}$$

This formulation is more relevant for our discussion, as it immediately highlights the symmetry of Ψ, as well as the soft constraints applied to it. The details of the reparametrization are shown in Appendix A.

Note that Eq. (6) may also be rewritten in the form (correct up to an additive constant term)

$$V = (\eta + \omega)(|\psi_1|^4 + |\psi_2|^4) + 2(\eta - \omega)|\psi_1|^2 |\psi_2|^2. \tag{7}$$

Comparing with Eq. (2), we have $g_{11} = g_{22} \equiv g = \eta + \omega$ and $g_{12} = \eta - \omega$. The model features repulsive intercomponent interactions provided $\eta - \omega > 0$, and this is the case we will mainly focus on. We will however briefly touch upon the case $\eta - \omega < 0$ corresponding to an attractive intercomponent density-density interaction, which leads to ground states with overlapping vortices in components 1 and 2. Normalizability of the individual order-parameter components, or equivalently boundedness from below of the free energy, requires that $\eta + \omega > 0$. Thus, while $\omega > \eta$ makes physical sense, $\omega < -\eta$ does not. In this paper, we assume $\eta > 0$ and $\omega \geqslant 0$.

Two-component BECs feature considerably richer physics than a single-component BEC. Since the gauge field parametrizing the rotation of the system is nonfluctuating, there is no gauge-field-induced current-current interaction between the two condensates (unlike in multicomponent superconductors). The only manner in which the two superfluid condensates interact is via the intercomponent density-density interaction $2(\eta - \omega)|\psi_1|^2|\psi_2|^2$. In the limit where the amplitudes of each individual component are completely frozen and uniform throughout the system, one recovers the physics of two decoupled 3D XY models, with a global U(1) × U(1) symmetry. The density-density interaction between ψ_1 and ψ_2 leads to interactions between the topological defects excited in each component. As a result, a first-order melting of two decoupled hexagonal lattices is not the only possible phenomenon that could take place. Previous experiments and numerical studies have reported a structural change of the ground state from a hexagonal to a square lattice of vortices as the effective intercomponent coupling is increased [5–7]. This corresponds

to increasing the ratio η/ω in our case. As we will see below, other unusual phenomena can also occur, notably when thermal fluctuations are included.

One special case of the model deserves some extra attention. If one takes the limit $\omega \to 0$ in Eq. (6) the symmetry of the model is expanded to a global SU(2) symmetry. One may then shift densities from one component to the other with impunity, as long as $|\psi_1|^2 + |\psi_2|^2$ is left unchanged. This effectively leads to massless amplitude fluctuations in the components of the order parameter. Therefore, it is possible to unwind a 2π phase winding in one component by letting the amplitude of the same component vanish. The introduction of this higher symmetry leads to very different vortex ground states than what are found in the $[\mathrm{U}(1) \times \mathrm{U}(1)]$-symmetric case with $\omega \neq 0$.

B. Separation of variables

In multicomponent GL models complex objects, such as combinations of vortices of different colors, are often of interest. In general, it is possible to rewrite an N-component model coupled to a gauge field, fluctuating or not, in terms of one mode coupled to the field and $N-1$ neutral modes [39,40]. For a more general discussion of charged and neutral modes in the presence of amplitude fluctuations see Refs. [41] and [42]. Considering only the kinetic part of the two-component Hamiltonian H_k, we have the following expression:

$$H_k = \frac{1}{2|\Psi|^2}|\psi_1^*\partial_\mu\psi_1 + \psi_2^*\partial_\mu\psi_2 - iA_\mu|\Psi|^2|^2 + \frac{1}{2|\Psi|^2}|\psi_1\partial_\mu\psi_2 - \psi_2\partial_\mu\psi_1|^2. \tag{8}$$

Hence, the first mode couples to the applied rotation, while the second does not. This corresponds to the phase combinations $\theta_1 + \theta_2$ and $\theta_1 - \theta_2$, respectively.

C. Lattice regularization

In order to perform simulations of the continuum model, we define the field Ψ on a discrete set of coordinates, i.e., $\Psi(\mathbf{r}) \to \Psi_{\mathbf{r}}$, where $\mathbf{r} \in (i\hat{\mathbf{x}} + j\hat{\mathbf{y}} + k\hat{\mathbf{z}}|\ i,j,k = 1,\ldots,L)$. Here, L is the linear size in all dimensions; the system size is $V = L^3$. We use periodic boundary conditions in all directions. By replacing the differential operator by a gauge-invariant forward difference

$$\left(\frac{\partial}{\partial r_\mu} - iA_\mu(\mathbf{r})\right)\Psi(\mathbf{r}) \to \frac{1}{a}(\Psi_{\mathbf{r}+a\hat{\boldsymbol{\mu}}}e^{-i(2\pi/\Phi_0)aA'_{\mu,\mathbf{r}}} - \Psi_{\mathbf{r}}), \tag{9}$$

and introducing real phases and amplitudes $\psi_{\mathbf{r},i} = |\psi_{\mathbf{r},i}|e^{i\theta_{\mathbf{r},i}}$ we can rewrite the Hamiltonian:

$$H = \sum_{\substack{\mathbf{r},\hat{\boldsymbol{\mu}}\\ i}} |\psi_{\mathbf{r}+\hat{\boldsymbol{\mu}},i}||\psi_{\mathbf{r},i}|\cos(\theta_{\mathbf{r}+\hat{\boldsymbol{\mu}},i} - \theta_{\mathbf{r},i} - A_{\mu,\mathbf{r}}) + \sum_{\mathbf{r}} V(\Psi_{\mathbf{r}}). \tag{10}$$

The lattice spacing is chosen so that it is smaller than the relevant length scale of variations of the amplitudes. A dimensionless vector potential A_μ has also been introduced. See Appendix A for details. We denote the argument of the cosine as $\chi^\mu_{\mathbf{r},i}$, as a shorthand.

D. Observables

An important and accessible quantity when exploring phase transitions is the specific heat of the system,

$$c_V = \beta^2\frac{\langle H^2\rangle - \langle H\rangle^2}{L^3}. \tag{11}$$

While crossing a first-order transition there is some amount of latent heat in the system, manifesting itself as a δ-function peak of the specific heat in the thermodynamic limit. On the lattice one expects to see a sharp peak, or anomaly, at the transition. This is used to characterize the transition as first order.

A useful measure of the global phase coherence of the system is the helicity modulus, which is proportional to the superfluid density. It serves as a probe of the transition from a superfluid to a normal fluid. In the disordered phase, the moduli in all directions are zero, characterizing an isotropic normal-fluid phase. The cause of this is a vortex loop blowout. Moving to the ordered phase, all moduli evolve to a finite value. If we turn on the external field we still have zero coherence in all directions in the disordered phase. In the ordered phase, however, the helicity modulus along the direction of the applied rotation jumps to the finite value through a first-order transition. The value of the transverse moduli will remain zero. Formally, the helicity modulus is defined as a derivative of the free energy with respect to a general, infinitesimal phase twist along r_μ [43]. That is, we perform the replacement

$$\theta_{\mathbf{r},i} \to \theta'_{\mathbf{r},i} = \theta_{\mathbf{r},i} - b_i\delta_\mu r_\mu \tag{12}$$

in the free energy, and calculate

$$\Upsilon_{\mu,(b_1,b_2)} = \left.\frac{\partial^2 F[\theta']}{\partial\delta_\mu^2}\right|_{\delta_\mu=0}. \tag{13}$$

Here, $b = (b_1,b_2)$ represents some combination of the phases θ_1 and θ_2, $b_1\theta_1 + b_2\theta_2$. To probe the individual moduli, b_i is chosen as $b_i = (1,0)$ or $b_i = (0,1)$. The composite phase-sum variable is represented by the choice $b_i = (1,1)$, while $b_i = (1,-1)$ is the phase difference. Generally, for a two-component model, the helicity modulus can be written as the sum of two indivudual moduli and a cross term [36,40],

$$\Upsilon_{\mu,(b_1,b_2)} = b_1^2\Upsilon_{\mu,(1,0)} + b_2^2\Upsilon_{\mu,(0,1)} + 2b_1b_2\Upsilon_{\mu,12}. \tag{14}$$

For the model considered in this paper, the individual helicity moduli can be written as

$$\langle\Upsilon_{\mu,i}\rangle = \frac{1}{V}\left[\left\langle\sum_{\mathbf{r}}\psi_{\mathbf{r}_i}\psi_{\mathbf{r}+\hat{\boldsymbol{\mu}},i}\cos\left(\chi^\mu_{\mathbf{r},i}\right)\right\rangle - \beta\left\langle\left(\sum_{\mathbf{r}}\psi_{\mathbf{r},i}\psi_{\mathbf{r}+\hat{\boldsymbol{\mu}},i}\sin\left(\chi^\mu_{\mathbf{r},i}\right)\right)^2\right\rangle\right], \tag{15}$$

while the mixed term has the form

$$\langle \Upsilon_{\mu,12} \rangle = -\beta \left\langle \left(\sum_{\mathbf{r}} |\psi_{\mathbf{r},1}||\psi_{\mathbf{r}+\hat{\boldsymbol{\mu}},1}| \sin\left(\chi^{\mu}_{\mathbf{r},1}\right) \right) \times \left(\sum_{\mathbf{r}} |\psi_{\mathbf{r},2}||\psi_{\mathbf{r}+\hat{\boldsymbol{\mu}},2}| \sin\left(\chi^{\mu}_{\mathbf{r},2}\right) \right) \right\rangle. \quad (16)$$

We denote the helicity modulus of the phase sum $\Upsilon_{\mu,(1,1)}$ as Υ^{+}_{μ} as a shorthand.

The structure factor $S_i(\mathbf{q}_\perp)$ can be used to determine the underlying symmetry of the vortex lattice. Square and hexagonal vortex structures will manifest themselves as four or six sharp Bragg peaks in reciprocal space. In a vortex liquid phase one expects a completely isotropic structure factor. The structure factor is defined as the Fourier transform of the longitudinally averaged vortex density $\langle n_i(\mathbf{r}_\perp)\rangle$, which is subsequently thermally averaged,

$$S_i(\mathbf{q}_\perp) = \frac{1}{L_x L_y f} \left\langle \left| \sum_{\mathbf{r}_\perp} n_i(\mathbf{r}_\perp) e^{-i\mathbf{r}_\perp \cdot \mathbf{q}_\perp} \right| \right\rangle. \quad (17)$$

Here $n_i(\mathbf{r}_\perp)$ is the density of vortices of color i averaged over the z direction,

$$n_i(\mathbf{r}_\perp) = \frac{1}{L_z} \sum_z n_i(\mathbf{r}_\perp, z), \quad (18)$$

and $\mathbf{r}_\perp$ is $\mathbf{r}$ projected onto a layer of the system with a given z coordinate. The vortex density is calculated by traversing each plaquette of the lattice, adding the factor $\chi^{\mu}_{i,\mathbf{r}}$ of each link. Each time we have to add (or subtract) a factor of 2π in order to bring this sum back into the primary interval of $(-\pi,\pi]$ a vortex of color i and charge $+1$ (-1) is added to this plaquette.

In addition to the structure factor, we look at thermally averaged vortex densities $\langle n_i(\mathbf{r}_\perp)\rangle$ as well as thermally and longitudinally averaged amplitude densities $\langle |\psi_i|^2(\mathbf{r}_\perp)\rangle$, defined similarly to Eq. (18),

$$|\psi_i|^2(\mathbf{r}_\perp) = \frac{1}{L_z} \sum_z |\psi_i|^2(\mathbf{r}_\perp, z). \quad (19)$$

This provides an overview of the real-space configuration of the system.

When including amplitude fluctuations, which, when the potential term is disregarded, are unbounded from above, it is of great importance to make sure all energetically allowed configurations are included. To this end, we measured the probability distribution of $|\psi_i|^2$, $P(|\psi_i|^2)$ during the simulations by making a histogram of all field configurations at each measure step, and normalizing its underlying area to unity in postprocessing.

The uniform rotation applied to the condensates is implemented in the Landau gauge:

$$\mathbf{A} = (0, 2\pi f x, 0), \quad (20)$$

where f is the density of vortices in a single layer. Note that this implies a constraint $Lf \in (1,2,3,\ldots)$ due to the periodic boundary conditions. When probing a first-order melting transition, it is important to choose a filling fraction large enough that an anomaly in the specific heat is detectable. However, if the filling fraction is too large, one may transition directly from a vortex liquid into a pinned solid, completely missing the *floating solid* phase of interest. This scenario is characterized by a sharp jump in not only the longitudinal, but also the transverse helicity modulus [44,45]. One must therefore chose f small enough to assure that the vortex line lattice is in a floating solid phase when it melts.

III. DETAILS OF THE MONTE CARLO SIMULATIONS

The simulations were performed using the Metropolis-Hastings algorithm [46,47]. Phase angles were defined as $\theta \in (-\pi,\pi]$, and amplitudes as $|\psi|^2 \in (0, 1+\delta\psi]$. The choice of $\delta\psi$ will be discussed further, as it is important to ensure inclusion of the full spectrum of fluctuations. Both the phases and the amplitudes were discretized to allow the use of tables for trigonometric and square root functions in order to speed up computations. We typically simulated systems of size $L^3 = 64^3$, with sizes up to $L^3 = 128^3$ used to resolve anomalies in the specific heat. We used 10^6 Monte Carlo sweeps per inverse temperature step, and up to 10^7 close to the transition. 10^5 additional sweeps were typically used to thermalize the system. In the simulations, we examined time series of the internal energies taken during both the thermalization runs and the measurement runs to make sure the simulation converged. One sweep consists of picking a new random configuration for each of the four field variables separately in succession, at each lattice site. Measurements were usually performed with a period of 100 sweeps, in order to avoid correlations. Ferrenberg-Swendsen multihistogram reweighting was used to improve statistics around simulated data points, and jackknife estimates of the errors are used.

Figure 1 shows the probability distribution of the amplitudes, $\mathcal{P}(|\psi_i|^2)$. We get a peaked distribution for finite ω. On the other hand, when $\omega = 0$, this is no longer the case. The distribution now approaches a uniform distribution on the interval $(0,1]$. In this case the parameter η serves to control

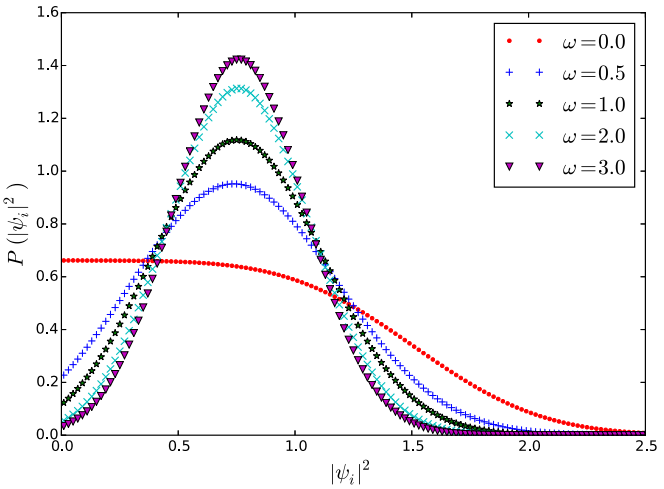

FIG. 1. (Color online) The probability distribution of the amplitudes, $\mathcal{P}(|\psi_i|^2)$, for $N = 2$, at inverse temperature $\beta = 1.20$, $f = 1/32$, and $\eta = 2$, with ω values from 0 to 3. The distribution is completely symmetric in i.

the approach to uniformity, $\eta \to \infty$ corresponding to the CP^1 limit.

With these initial simulation runs as a basis, we choose $\delta\psi$ appropriately in order to capture the entire spectrum of fluctuations.

IV. RESULTS OF THE MONTE CARLO SIMULATIONS

In this section, the η-ω phase diagram of ground states is explored by slow cooling and examination of vortex and amplitude densities, as well as structure factors. In addition to the expected hexagonal and square vortex ground states, several interesting regions of the parameter space are investigated further. A special case between the square and the hexagonal regions of the phase diagram is discovered, where the lattice first forms a square structure, but thermally reconstructs into a hexagonal lattice as the temperature is decreased further. Furthermore, we consider in detail the $\omega = 0$ line in the phase diagram, where we discover additional vortex fluctuation effects. For $\omega = 0$, the system features an SU(2) symmetry. An unusual feature is an interesting state with global phase coherence, but without a regular vortex lattice. In this case ordinary vortices do not have topological character due to SU(2) symmetry. Additionally, we obtain several interesting vortex structures characterized by dimerlike configurations at lower temperatures. Here, we observe honeycomb lattices, or double-core lattices, and stripe configurations, consistent with previous $T = 0$ results [6].

We also examine the melting transitions of the square and hexagonal lattices with the full amplitude distribution included, as well as the melting of the hexagonal lattice in a model with $N = 1$ as a benchmark of the method. To classify the transition, we look at thermal averages of the specific heat, helicity moduli, and vortex structure factors. These results are presented in Appendixes B and C.

A. The η-ω phase diagram

Adding a second matter field and intercomponent density-density interactions results in a considerably richer set of ground states than in the single-component case. In the absence of a fluctuating part of the rotational "gauge field" there will be no gauge-field-mediated intercomponent current-current interactions. For $\eta - \omega < 0$ ($\eta,\omega > 0$) the effective intercomponent density-density coupling $\eta - \omega$ is negative and the ground state of each color of condensate has a hexagonal symmetry, as shown in Fig. 2(a). If, on the other hand $\eta - \omega > 0$, the intercomponent coupling becomes positive. Now, for sufficiently large ratios η/ω, the vortices arrange themselves into two interpenetrating square lattices, shown in Fig. 2(b). The value of the ratio η/ω for which the lattice reconstructs depends on the strength of the rotation f. If we neglect fluctuations, $\eta - \omega < 0$ is expected to result in a hexagonal lattice, while $\eta - \omega > 0$ leads to a square lattice for sufficiently large η/ω.

The physics of the reconstruction of the lattice can be explained by modulations of the amplitude fields. The existence of static periodic amplitude modulations (density variations) is due to the presence of vortices. Without vortices ($f = 0$) and $\omega > 0$, the ground state is one where both amplitudes are

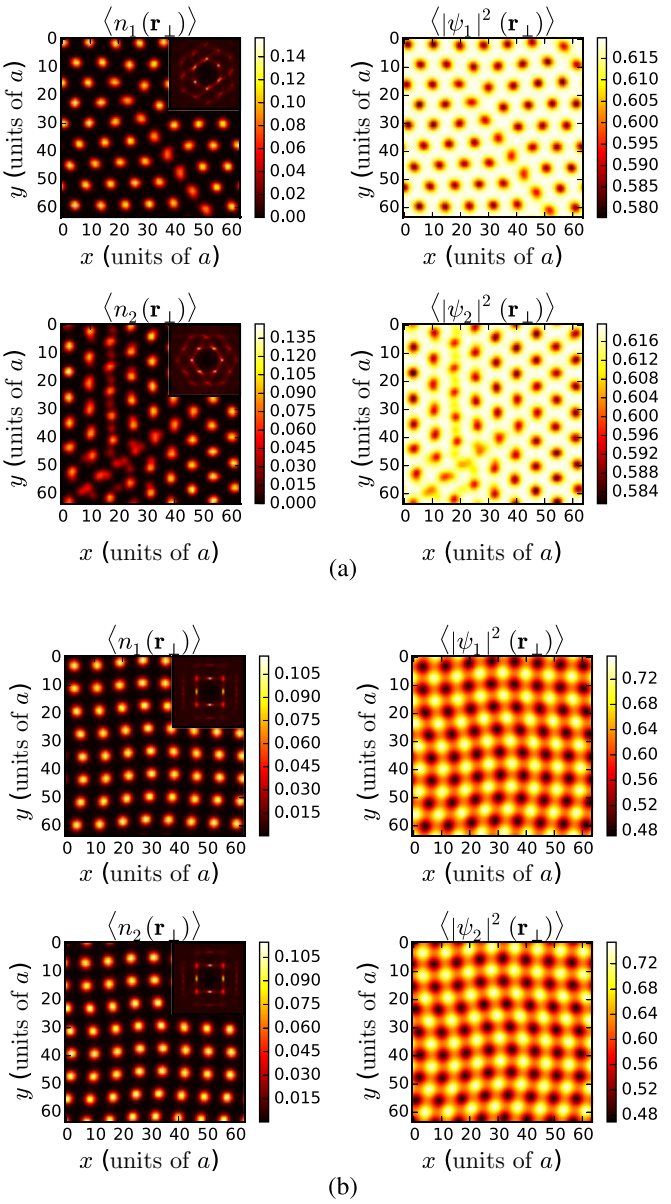

FIG. 2. (Color online) Representative configurations of the two main ordered phases in the U(1) × U(1) region. (a) shows a square structure at $(\eta,\omega) = (5.0,0.5)$, while (b) illustrates the hexagonal structure at $(\eta,\omega) = (5.0,5.0)$. Each subfigure shows vortex densities $\langle n_i(\mathbf{r}_\perp)\rangle$ in the left column, amplitude densities $\langle|\psi_i|^2(\mathbf{r}_\perp)$ in the right column, and structure factors (insets) of each component as indicated. The induced vortex density and inverse temperature are fixed to $f = 1/64$ and $\beta = 1.5$ in both subfigures.

equal and smooth. Vortices in one component tend to suppress locally the corresponding amplitude, which in turn means that the term $\eta(|\psi_1|^2 + |\psi_2|^2 - 1)^2$ enhances the amplitude of the other component. At small ω, i.e., large $\eta - \omega$, there is a strong tendency to form a square density lattice due to this intercomponent density-density interaction. Conversely, if ω is large enough compared to η, the density-density interaction is not strong enough to overcome the isotropic current-current interactions between same-species vortices. In other words if the current-current interactions dominate the interspecies density-density interactions, a hexagonal lattice is

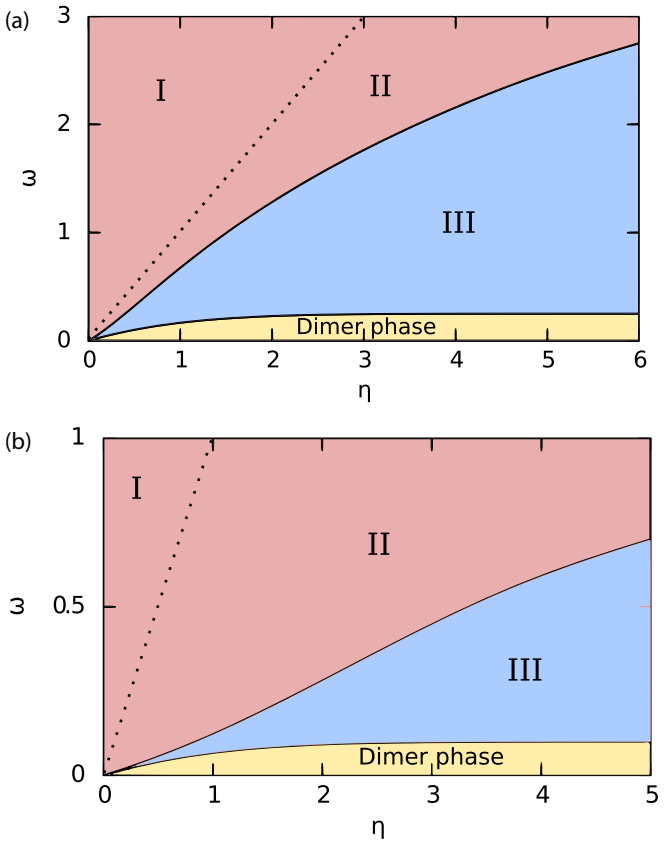

FIG. 3. (Color online) The η-ω phase diagram of the ground states for $f = 1/32$ (a) and $f = 1/64$ (b). The simulations were performed for a range of (η,ω) pairs to determine the zero-temperature ground state. Approximate demarcation lines for the phase boundaries separating hexagonal lattices, square lattices, and dimerized phases, were drawn from these results (solid lines). I denotes the phase where the hexagonal vortex lattices in the two components are cocentric, II denotes the case where the hexagonal lattices are intercalated, while III denotes the square lattice phase. The dotted line is the line $\omega = \eta$ at which the intercomponent density-density interaction $2(\eta - \omega)|\psi_1|^2|\psi_2|^2$ changes sign. See also Figs. 11 and 12 in Appendix D.

energetically favored over a square lattice, and vice versa. Note that similarly a square vortex lattice forms in two-component London models with dissipationless drag when there are competing inter- and intraspecies current-current vortex interactions [34,35].

Figures 3(a) and 3(b) show the phase diagrams for filling fractions $f = 1/32$ and $f = 1/64$, respectively. The separation line is approximate and drawn from several separate simulations.

To clarify what is going in Figs. 3(a) and 3(b), we refer to Figs. 11 and 12 in Appendix D. Here, we show tableaus to illustrate in more detail how the density and vortex lattices reconstruct at a temperature well below any melting temperatures of the vortex (and density) lattices, as the density-density interaction $2(\eta - \omega)|\psi_1|^2|\psi_2|^2$ is varied. Specifically, we fix the interaction parameter η, as well as the inverse temperature β and filling fraction f, while increasing the parameter ω. This reduces the effective intercomponent density-density interaction which favors a square lattice, until the lattice reconstructs from square to hexagonal symmetry.

When $\eta = \omega$, it is seen from Eq. (7) that the two components of the order parameter decouple. For $\omega < \eta$ the intercomponent density-density interaction is repulsive, while it is attractive for $\omega > \eta$. For $\omega < \eta$, the vortex lattices (and the density lattices) are intercalated, while for $\omega > \eta$ they are cocentric. In Figs. 3(a) and 3(b) we illustrate the demarcation line between the two situations as a dotted line in the hexagonal phase.

Beyond the square and hexagonal lattices we also observe dimer configurations of vortices for $\omega = 0$, which will be discussed further below. The calculations are consistent with the ground states obtained in Refs. [6] and [10].

B. Thermally induced reconstruction of vortex lattices

Now we move to discussion of the effects of thermal fluctuations in these systems. Figure 4 shows the vortex densities in component 1 in reciprocal space, as β is increased, i.e., as temperature is reduced, in a temperature range below where the lattice melts. The actual melting of the two-component lattice is discussed in Sec. IV C. We fix the filling fraction $f = 1/64$, as well as the interaction parameters $\eta = 2$ and $\omega = 0.5$.

For the highest temperatures shown in Fig. 4 the vortex lattice is square. Upon cooling the system, the vortex lattice reconstructs into a hexagonal lattice, consistent with the ground-state phase diagram of Fig. 3(b). The density-density interaction term $2(\eta - \omega)|\psi_1|^2|\psi_2|^2$ aids formation of a square lattice at higher temperatures, while the current-current interactions drive the lattice towards a hexagonal configuration when it is cooled further. This means that the free energy per vortex of the square lattice, which is lower than that of the hexagonal lattice at $\beta = 0.90$, has become larger than that of the hexagonal lattice when $\beta = 1.50$. This is essentially the combination of an energetic and an entropic effect. We observe this reconstruction not too far away from the demarcation line separating a square and a hexagonal vortex lattice. Deep inside the hexagonal phase in Fig. 3(b), we observe direct vortex lattice melting from a hexagonal lattice to a vortex liquid. We note that intermediate entropically stabilized vortex lattice phases were a subject of interesting investigation in the different system of U(1) × U(1) superconductors [48]; however, the vortex interaction form is different in our case.

C. SU(2) vortex states

The limit $\omega \to 0$ is quite different from the [U(1) × U(1)]-symmetric case $\omega \neq 0$. From Eq. (6), it is seen that the Hamiltonian is invariant under SU(2) transformations of Ψ. Vortices, which are topological in a U(1) × U(1) model, are no longer topological in the SU(2) case. One may unwind a 2π phase winding by entirely transferring density of one component to the other, which may be done at zero energy cost.

Figure 5 shows one of the main results of this paper. These are simulations with SU(2) symmetry, i.e., $\omega = 0$, as well as $\eta = 5.0$ and $f = 1/64$. The top panel show the phase stiffness associated with the phase sum, Υ_μ^+. This is the physically relevant phase variable in this case, as it couples to the rotation.

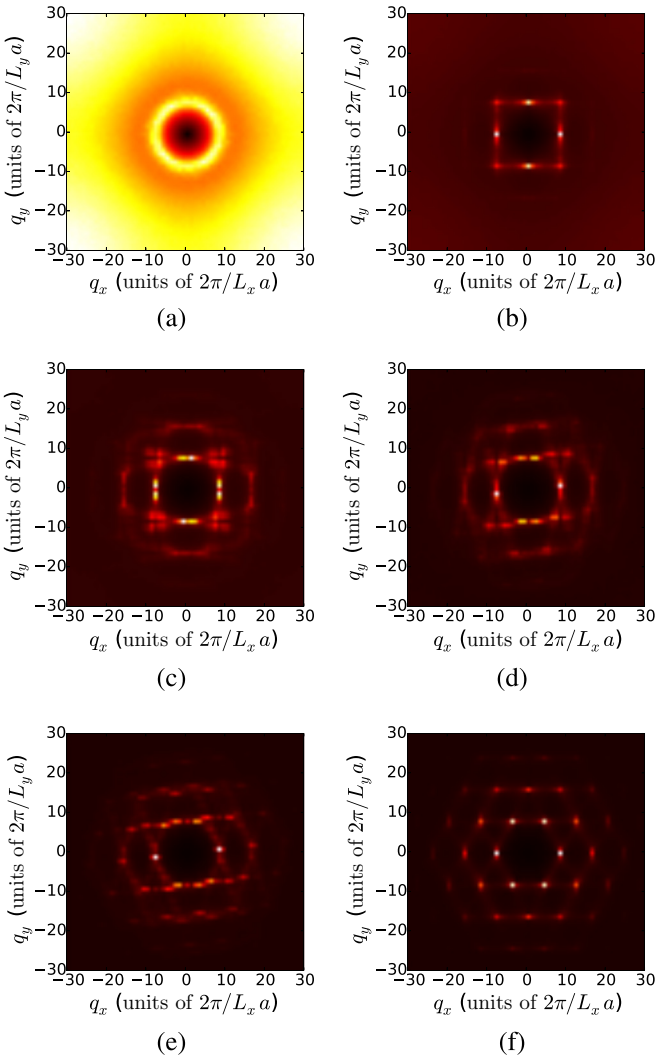

FIG. 4. (Color online) Thermally induced reconstruction from a square vortex lattice in either of the components at $\eta = 2, \omega = 0.5$, to a hexagonal vortex lattice, as β is increased. Here, $f = 1/64$. (a)–(f) show inverse temperatures $\beta = \{0.80, 0.90, 1.20, 1.30, 1.34, 1.38\}$, respectively. Each subfigure shows $S_1(\mathbf{q}_\perp)$ only; $S_2(\mathbf{q}_\perp)$ is identical. The physical reason for the reconstruction originates with the inter-component density-density interaction term $2(\eta - \omega)|\psi_1|^2|\psi_2|^2$), and is explained in detail in the text.

We observe that the stiffness along the z direction becomes finite at an inverse temperature $\beta \sim 0.9$. This is what one would expect when a vortex lattice forms. However, the bottom panels, which show the vortex density of component 1 at $\beta = 0.94$, show no apparent signs of vortex ordering. Hence, we have an unusual situation. There is a relatively large β range where we have a finite z-directed helicity modulus of the phase sum, but no apparent ordering of induced vortices. A finite helicity modulus generally means that there are straight vortex lines with very little transverse fluctuations threading the entire system along the direction in question. In the U(1) picture this corresponds to a regular vortex lattice. For an SU(2) condensate, this is no longer the case. Large relative amplitude fluctuations can occur since they have zero energy cost in the ground state as the energy is no longer minimized by a preferential value of $|\psi_1|^2 - |\psi_2|^2$. This results in many

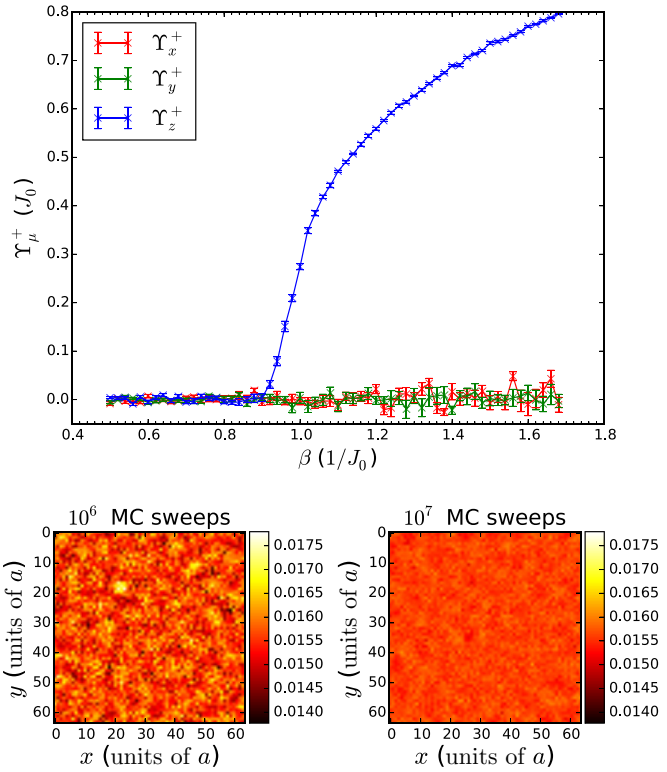

FIG. 5. (Color online) Illustration of the observed state with coherence along the direction of the rotation axis without a regular vortex lattice, seen only with SU(2) symmetry. The parameters used are $\omega = 0.0$, $\lambda = 5$, and $f = 1/64$. The top panel shows the helicity modulus of the phase sum, Υ_μ^+. The two bottom panels show the vortex densities $n_1(\mathbf{r}_\perp)$ at $\beta = 0.94$, where the z-directed modulus is clearly finite. The bottom left and bottom right panels are taken from simulations using 10^6 and 10^7 Monte Carlo sweeps, respectively. No apparent vortex line structure is seen here, and by increasing the number of Monte Carlo sweeps the variations of the vortex density are smoothed out further. Note how the value of the average vortex density seems to converge towards $1/64$.

(nearly) degenerate vortex states between which the system can fluctuate, thus greatly simplifying the effort of moving an entire, almost straight, vortex line. We are left with a phase where we have coherence along the z direction, but no regular vortex lattice appears in thermal averages. Nearly straight vortex lines will shift between a large number of degenerate, or nearly degenerate, states at a time scale shorter than a typical Monte Carlo run.

The bottom panels of Fig. 5 show some inhomogeneities of the vortex densities, exemplifying that this is not an ordinary vortex liquid with segments of vortex lines executing transverse meanderings along their direction, which would yield zero helicity modulus along the direction of the field-induced vortices. Rather, what we have is a superposition of many latticelike states of nearly straight vortex lines, where the fluctuations are largely collective excitations of entire nearly straight lines, rather than fluctuations of smaller segments of lines.

We emphasize again that these collective excitations originate with large amplitude fluctuations due to the SU(2) softness of the amplitudes of the components of the superfluid order parameter, rather than with phase fluctuations. Increasing the

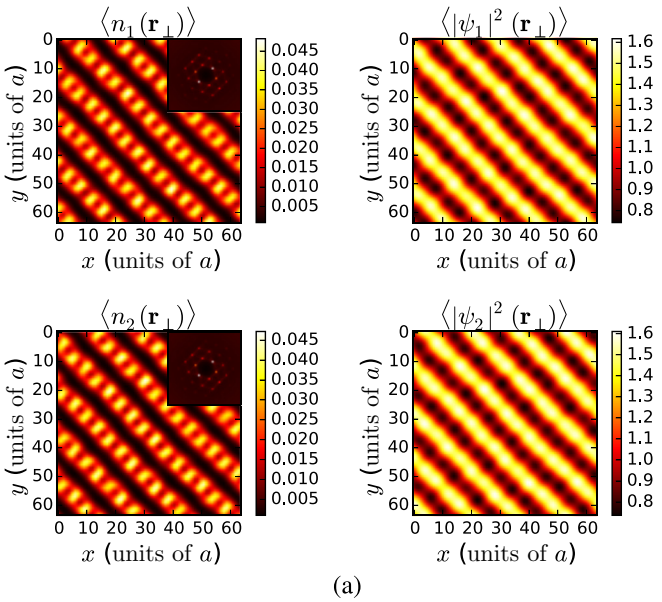

(a)

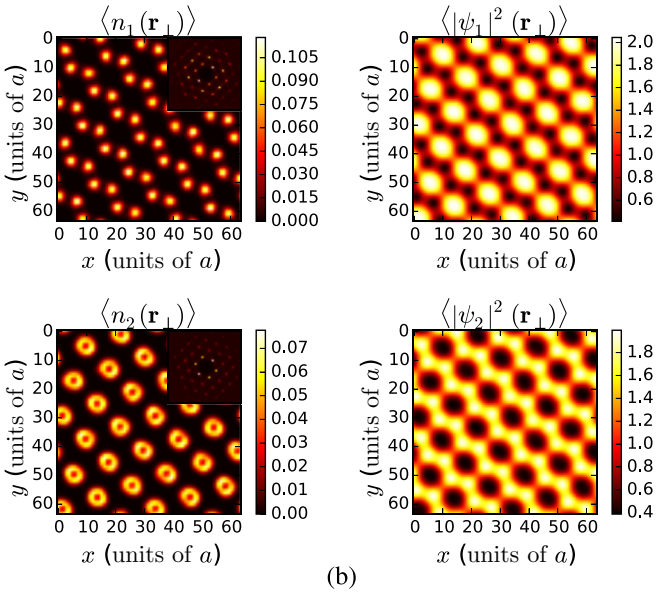

(b)

FIG. 6. (Color online) Two examples of SU(2) vortex configurations from a single simulation, for two different inverse temperatures. The parameters η, f, and ω are fixed in each subfigure, at $\eta = 1.0$, $\omega = 0.0$, and $f = 1/64$. (a) shows $\beta = 0.84$, while (b) shows $\beta = 1.50$. Each subfigure shows vortex densities $\langle n_i(\mathbf{r}_\perp)\rangle$ in the left column, amplitude densities $\langle|\psi_i|^2(\mathbf{r}_\perp)\rangle$ in the right column, and structure factors (insets) of each component as indicated. This illustrates the degeneracy of the vortex line lattice in the isotropic limit, as the configurations evolve when β is varied. See Appendix D for more details.

number of Monte Carlo sweeps by an order of magnitude smooths these variations out (without noticably altering the value of Υ_z^+), as seen in the bottom right panel of Fig. 5. Note how the average value of the vortex density seems to converge towards $1/64$. This is what we expect for a vortex lattice or liquid in a [U(1) × U(1)]-symmetric model, as the density of thermal vortices will average to zero, and f is the average flux density per plaquette.

As the system is cooled further, the movements of large vortex lines cease, and a regular vortex lattice appears. However, degeneracy must still be present, as the exact pattern formed by the lattice is distinctively different between simulations (keeping all parameters equal). The lattice also has a tendency to shift between configurations as the temperature is varied, below the temperature of initial vortex-lattice formation. We observe two distinct classes of vortex states, illustrated in Fig. 6. The two are stripes [Fig. 6(a)] and honeycomb lattices [Fig. 6(b)], both of which are seen in Ref. [6]. Note that these vortex densities are taken from a single simulation, after the lattice has formed. Within the accuracy of our simulations the obtained states are not metastable. The evidence of this is obtained by performing several independent runs from different initial configurations. Again, we refer to Appendix D, where Fig. 13 illustrates the degeneracy in the vortex line lattices obtained in the isotropic limit in further detail.

V. EXPERIMENTAL CONSIDERATIONS

Hexagonal and square lattices have already been observed in binary condensates of rubidium [7]. However, an SU(2) condensate has not been realized experimentally. In this section, we briefly outline under what circumstances an observation of an SU(2) vortex state may be feasible.

In order to experimentally realize SU(2) conditions, one requires a two-component BEC, where both intra- and intercomponent interactions are equal. As we have seen, the SU(2) physics crucially depends on this, since even minor deviations from this condition immediately yield U(1) × U(1) physics. This corresponds to $\omega = 0$ in our parametrization. Intra- and intercomponent density-density interactions are given in terms of scattering lengths. While tuning of these in an experiment is possible with Feshbach resonances, it may still be a challenge to tune two scattering lengths independently to be equal to a third, to arrive at the SU(2) point. From what is known for scattering lengths of real systems, it appears that a mixture of two species of the same atom, but in different hyperfine states, lends itself more readily to a realization of an SU(2) condensate than a mixture of different atoms or a mixture of different isotopes of the same atom. This is so, since in the former case, the relevant scattering lengths typically *a priori* are much more similar to each other than they are in more heterogeneous mixtures.

One promising candidate therefore appears to be a condensate of ^{87}Rb prepared in the two hyperfine states $|F = 1, m_f = 1\rangle \equiv |1\rangle$ and $|F = 2, m_f = -1\rangle \equiv |2\rangle$. In this system, the three relevant s-wave scattering lengths already have values close to the point of interest, $a_{11} = 100.4a_B$, $a_{22} = 95.00a_B$, and $a_{12} = 97.66a_B$, where a_B is the Bohr radius [2,49]. Reference [11] reports on a *magnetic* Feshbach resonance at a field of approximately 9.1 G, where control of a_{12} of the order of $10a_B$ is possible. Additionally, Ref. [50] reports on an *optical* Feshbach resonance of the state $|F = 1, m_F = -1\rangle$, able to tune the intracomponent scattering length, using two Raman lasers, with detuning parameters approximately given by $\Delta_1 = 2\pi \times 75$ MHz and $\Delta_2 = 2\pi \times 20$ MHz. Here, varying Δ_2 tunes the value of the scattering length around the Feshbach resonance, while varying Δ_1 changes the width. Hence, greater control of the resonance is possible with an

optical Feshbach resonance compared to a magnetic one. Presumably, there should exist optical Feshbach resonances able to tune the scattering length of either the $|1\rangle$ or the $|2\rangle$ state, for instance the one reported to exist at 1007 G for the $|1\rangle$ state [51]. This resonance should be far enough away from the intercomponent resonance at 9.1 G to not cause any interference.

This suggests one possible setup. Namely, prepare a two-component condensate of ^{87}Rb in the $|1\rangle$ and $|2\rangle$ states under rotation, and tune a_{12} to a_{22} using a magnetic field. Then, tune a_{11} to the same value using optical techniques, while taking time-of-flight images of the condensate. The prediction is that as the system is tuned through the optical Feshbach resonance, one should observe a hexagonal composite vortex lattice at subresonance frequencies, the nonunique vortex ordering pattern, discussed above, at a frequency where all scattering lengths are equal, close to the optical Feshbach resonance, and finally the reappearance of a hexagonal vortex lattice at frequencies above the frequency where all lengths are equal (Fig. 6). The observation of a featureless rotating condensate would be a direct manifestation of the loss of topological character of U(1) vortices in the SU(2)-symmetric case. It would be interesting to study the dynamics of the vortex lattice in this case with methods like those used in [52]. For other discussions of SU(N) models in cold atoms see Refs. [53] and [54].

In actual experiments, a magnetic trap is used to confine the condensate in a given lateral region. The effect of this on thermal fluctuations in vortex matter has been studied in detail in previous theoretical works for the one-component case, without amplitude fluctuations [55,56]. The effect of the trap is to yield a maximum overall condensate density at the center of the trap, while depleting it towards the edge of the trap. As a result, the lattice melts more easily near the edge of the trap. As can be inferred from the work on single-component melting [55,56], the results of the present paper, where no inhomogeneity due to a magnetic trap has been accounted for, is therefore most relevant to the region close to the center of the trap.

VI. CONCLUSIONS

In this paper, we have investigated a two-component U(1) × U(1) and SU(2) Bose-Einstein condensate with density-density interaction under rotation at finite temperature, thereby extending previous works which calculated the zero-temperature ground state numerically. In the U(1) × U(1) case we report that thermal fluctuations can lead to a phase transition between hexagonal and square vortex lattices with increased temperature.

In the isotropic, SU(2), limit, we have observed an intermediate state of global phase coherence without an accompanying vortex lattice in the thermally averaged measurements. In addition, we observe a variety of dimerized vortex states, such as dimerized stripes and honeycomblike lattices, which exist for a wide range of temperature. These lattices could be observed in binary Bose-Einstein condensates in two separate hyperfine states, by precisely tuning the inter- and intracomponent scattering lengths to the SU(2) point through the use of Feshbach resonances.

ACKNOWLEDGMENTS

We thank Erich Mueller for useful discussions. P.N.G. thanks NTNU and the Norwegian Research Council for financial support. E.B. was supported by by the Knut and Alice Wallenberg Foundation through a Royal Swedish Academy of Sciences Fellowship, by the Swedish Research Council Grants No. 642-2013-7837 and No. 325-2009-7664, and by the National Science Foundation under the CAREER Award No. DMR-0955902, A.S. was supported by the Research Council of Norway, through Grants No. 205591/V20 and No. 216700/F20. This work was also supported through the Norwegian consortium for high-performance computing (NOTUR).

APPENDIX A: REWRITING THE GENERAL HAMILTONIAN

Here we present the details of rewriting Eq. (2) into Eq. (5), which is more suited for our purposes. We repeat the starting point here for convenience.

$$H = \int d^3r \left[\sum_{i=1}^{N} \sum_{\mu=1}^{3} \frac{\hbar^2}{2m_i} \left| \left(\partial_\mu - i \frac{2\pi}{\Phi_0} A'_\mu \right) \psi'_i \right|^2 + \sum_{i}^{N} \alpha'_i |\psi'_i|^2 + \sum_{i,j=1}^{N} g'_{ij} |\psi'_i|^2 |\psi'_j|^2 \right]. \tag{A1}$$

First, we scale the field variables and Ginzburg-Landau parameters, to obtain some dimensionless quantities:

$$\alpha'_i = \alpha_0 \alpha_i, \tag{A2}$$

$$g'_{ij} = g_0 g_{ij}, \tag{A3}$$

$$|\psi'_i| = \sqrt{\frac{\alpha_0}{g_0}} |\psi_i|. \tag{A4}$$

This gives us the Hamiltonian,

$$H = \frac{\alpha_0^2}{g_0} \int d^3r \left[\sum_{i=1}^{N} \sum_{\mu=1}^{3} \frac{\hbar^2}{2m_i \alpha_0} \left| \left(\partial_\mu - i \frac{\Phi_0}{2\pi} A'_\mu \right) \psi_i \right|^2 + \sum_{i}^{N} \alpha_i |\psi_i|^2 + \sum_{i,j=1}^{N} g_{ij} |\psi_i|^2 |\psi_j|^2 \right], \tag{A5}$$

which on the lattice reads

$$H = \frac{\alpha_0^2 a^3}{g_0} \sum_{\mathbf{r}} \left[\sum_{i=1}^{N} \sum_{\mu=1}^{3} \frac{\hbar^2}{m_i \alpha_0 a^2} \times [|\psi_{\mathbf{r},i}|^2 - |\psi_{\mathbf{r}+\hat{\boldsymbol{\mu}},i}||\psi_{\mathbf{r},i}| \cos(\theta_{\mathbf{r}+\hat{\boldsymbol{\mu}},i} - \theta_{\mathbf{r},i} - A_{\mu,\mathbf{r}})] + \sum_{i}^{N} \alpha_i |\psi_{\mathbf{r},i}|^2 + \sum_{i,j=1}^{N} g_{ij} |\psi_{\mathbf{r},i}|^2 |\psi_{\mathbf{r},j}|^2 \right], \tag{A6}$$

where a is the lattice constant, and we have introduced

$$A_\mu = \frac{2\pi}{\Phi_0} a A'_\mu. \tag{A7}$$

Next, we specialize to the case $N = 2$, $\alpha_1 = \alpha_2$, $g_{11} = g_{22} \equiv g$, and $m_1 = m_2$, and define a^2 to be equal to $\hbar^2/m\alpha_0$, which sets our length scale. Note that it should not be confused with the coherence length in the multicomponent case without intercomponent density-density interaction. For the definition of coherence lengths in the presence of multiple components and intercomponent density-density interactions, see Refs. [57] and [58]. The energy scale is defined as J_0 as follows:

$$J_0 = \frac{\alpha_0^2 a^3}{g_0}. \tag{A8}$$

The coupling parameters η and ω used in this paper are defined by comparing the potential term of Eq. (A6) to the form where the soft constraints $|\psi_1|^2 + |\psi_2|^2 = 1$ and $|\psi_1|^2 - |\psi_2|^2 = 0$ are implemented. Thus, we have

$$V(\Psi) = \eta(|\psi_1|^2 + |\psi_2|^2 - 1)^2 + \omega(|\psi_1|^2 - |\psi_2|^2)^2, \tag{A9}$$

with

$$\eta = -\frac{\alpha}{2} - \frac{3}{2}, \tag{A10}$$

$$\omega = \frac{g - g_{12}}{2}. \tag{A11}$$

The lattice version of the Hamiltonian reads

$$\begin{aligned} H = &\sum_{\substack{\mathbf{r},\hat{\boldsymbol{\mu}} \\ i}} |\psi_{\mathbf{r}+\hat{\boldsymbol{\mu}},i}||\psi_{\mathbf{r},i}|[\cos(\theta_{\mathbf{r}+\hat{\boldsymbol{\mu}},i} - \theta_{\mathbf{r},i} - A_{\mu,\mathbf{r}})] \\ &+ \sum_{\mathbf{r}} \eta(|\psi_1|^2 + |\psi_2|^2 - 1)^2 \\ &+ \sum_{\mathbf{r}} \omega(|\psi_1|^2 - |\psi_2|^2)^2. \end{aligned} \tag{A12}$$

This model will then have the following continuum form:

$$H = \int d^3r \left[\sum_i^N \frac{1}{2} \left|(\partial_\mu - iA_\mu)\psi_i\right|^2 + V(\Psi) \right]. \tag{A13}$$

APPENDIX B: FIRST-ORDER LATTICE MELTING FOR $N = 1$ RECONSIDERED

As a benchmark on simulations with amplitude fluctuations included, we verify the well-established first-order melting transition on this model with only a single component of the order-parameter field, in the presence of amplitude fluctuations. The added feature of the computation is that the complete amplitude-distribution function was utilized, through the methods described in Sec. III. In this case, the term in the potential proportional to ω in Eq. (6) is absent, and the potential reduces to

$$V(\Psi) = \eta(|\Psi|^2 - 1)^2. \tag{B1}$$

With amplitude fluctuations neglected, this model reduces to the much studied uniformly frustrated 3D XY model, with well-known results as mentioned in the Introduction of the paper. The model features a first-order phase transition manifested as a melting of the frustration-induced hexagonal lattice of vortices [16,18–25]. The fluctuations responsible for driving this transition are massless transverse phase fluctuations of the order parameter.

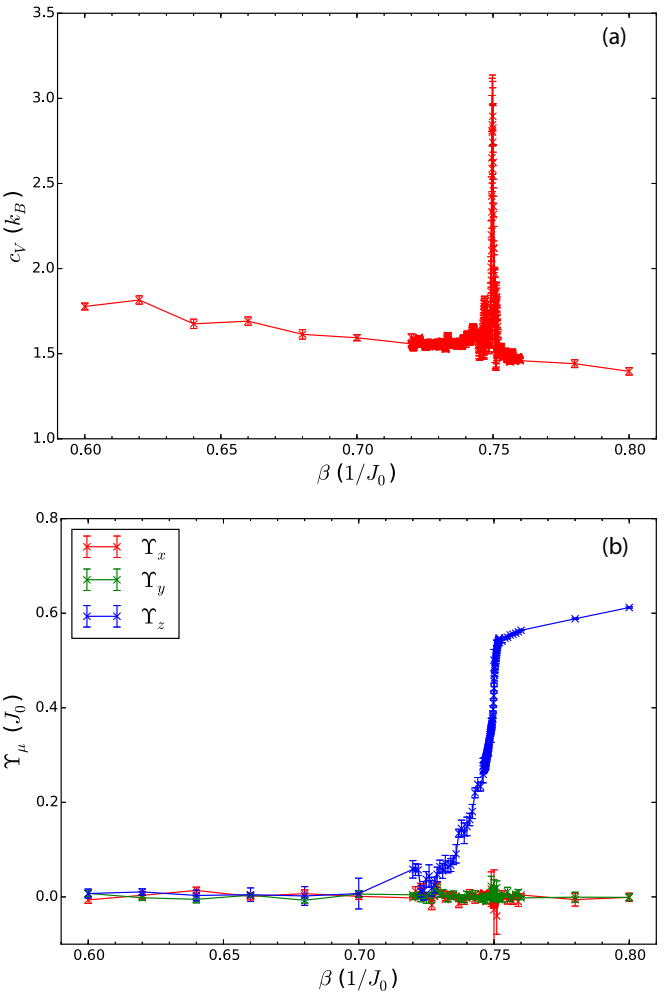

FIG. 7. (Color online) Specific heat (a) and helicity moduli (b) for $N = 1$, $f = 1/16$, and $\eta = 10$. At $\beta = 0.751$ we see a clear anomaly in the specific heat accompanied by a sharp jump in the longitudinal helicity modulus. The transverse moduli remain zero throughout the transition.

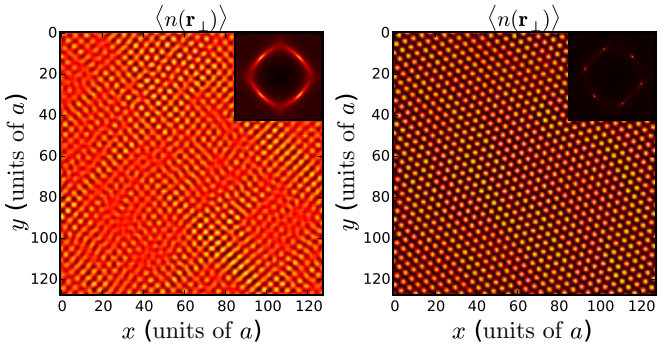

FIG. 8. (Color online) Vortex density $n(\mathbf{r}_\perp)$ and structure factor $S(\mathbf{q}_\perp)$ (inset) for $N = 1$, $f = 1/16$, and $\eta = 10$, at inverse temperatures $\beta = 0.749$ (left) and $\beta = 0.752$ (right). This corresponds to temperatures slightly higher and lower, respectively, than the transition point $\beta = 0.751$.

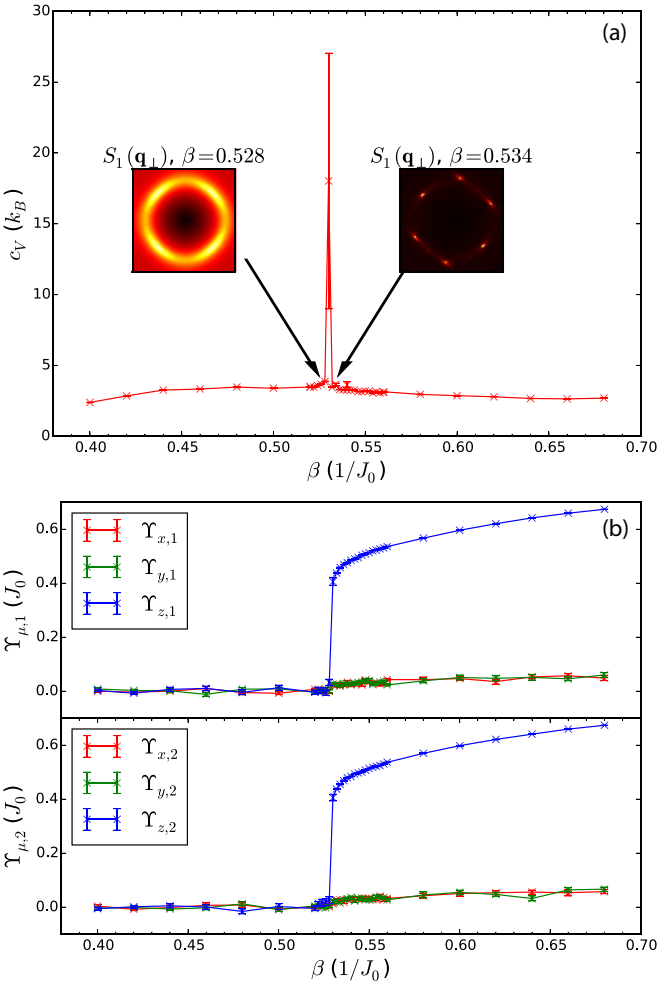

FIG. 9. (Color online) Specific heat (a) and helicity moduli of both components (b), for $N = 2$, $f = 1/16$, $\omega = 1.0$, and $\eta = 0.5$. At $\beta \approx 0.53$ we see a clear anomaly in the specific heat accompanied by a sharp jump in the longitudinal helicity moduli of both components. The transverse helicity moduli remain at zero throughout the transition. The insets in (a) show the structure factors at the high- and low-temperature sides of the transition, respectively, $\beta = 0.528$ and $\beta = 0.534$. This clearly shows that the sharp anomaly in the specific heat separates an isotropic phase from a phase with hexagonal order.

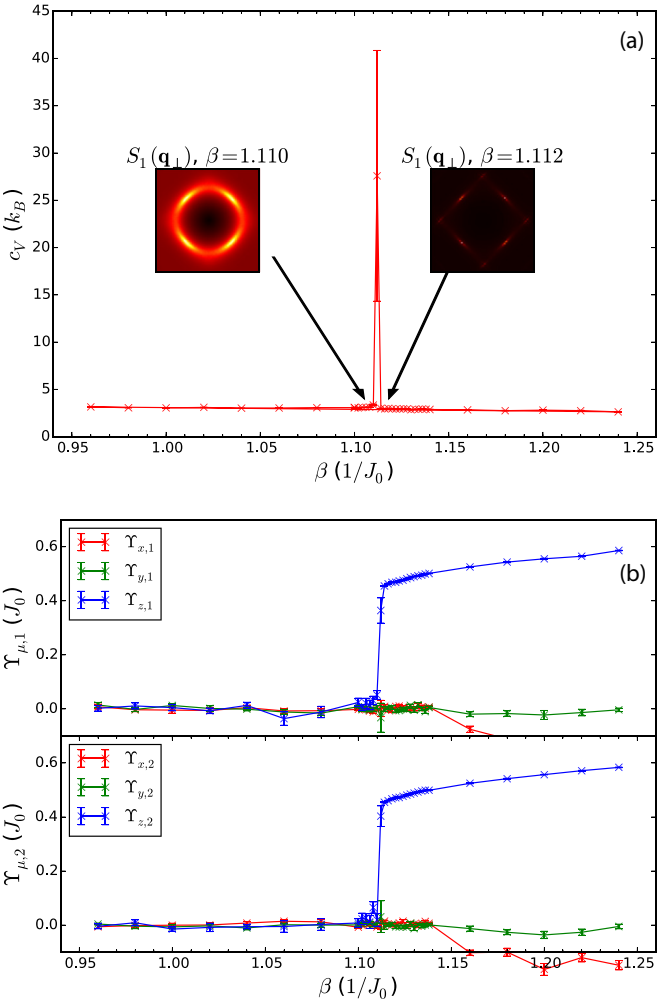

FIG. 10. (Color online) Specific heat (a) and helicity moduli of both components (b), for $N = 2$, $f = 1/16$, $\omega = 1.0$, and $\eta = 2.0$. At $\beta \approx 1.11$ we see a clear anomaly in the specific heat accompanied by a sharp jump in the longitudinal helicity moduli of both components. The transverse helicity moduli remain at zero throughout the transition, except for the x-directed modulus which drops to a negative value at a point well separated from the transition. The insets in (a) show the structure factors at the high- and low-temperature sides of the transition, respectively, $\beta = 1.110$ and $\beta = 1.112$. This clearly shows that the sharp anomaly in the specific heat separates an isotropic phase from a phase with square order.

The simulations were performed with $\eta = 10$. Figure 7(a) shows the specific heat, which has strong signs of an anomaly at $\beta = 0.751$. Figure 7(b) shows that the anomaly in the specific heat is accompanied by a relatively sharp jump in the helicity modulus in the z direction. It is also important to note that the helicity moduli in the transverse directions remain zero throughout the transition. This indicates that the vortex lattice melts in a genuine phase transition, and not as a result of thermal depinning from the underlying numerical lattice. This is therefore a strong indication of a first-order melting transition. Figure 8 shows the vortex density and structure factor immediately before and after the transition. The high-temperature side shows an incoherent vortex liquid, characterized by a circular structure factor. The low-temperature side shows that a clear hexagonal structure is established as soon as the liquid freezes.

We emphasize that these results are not unexpected. The purpose of including them here is to demonstrate that the method of including amplitude fluctuations into the computation of the vortex lattice melting reproduces the known result for $N = 1$, previously obtained in the absence of amplitude fluctuations [16,18–25], but generally believed to be correct also when amplitude fluctuations are included.

APPENDIX C: FIRST-ORDER LATTICE MELTING FOR $N = 2$

We next consider the melting transition for $N = 2$, where the intercomponent density-density interaction $2(\eta - \omega)|\psi_1|^2|\psi_2|^2$ term in the potential energy in Eq. (7) comes into play. We consider the $[U(1) \times U(1)]$-symmetric case, i.e.,

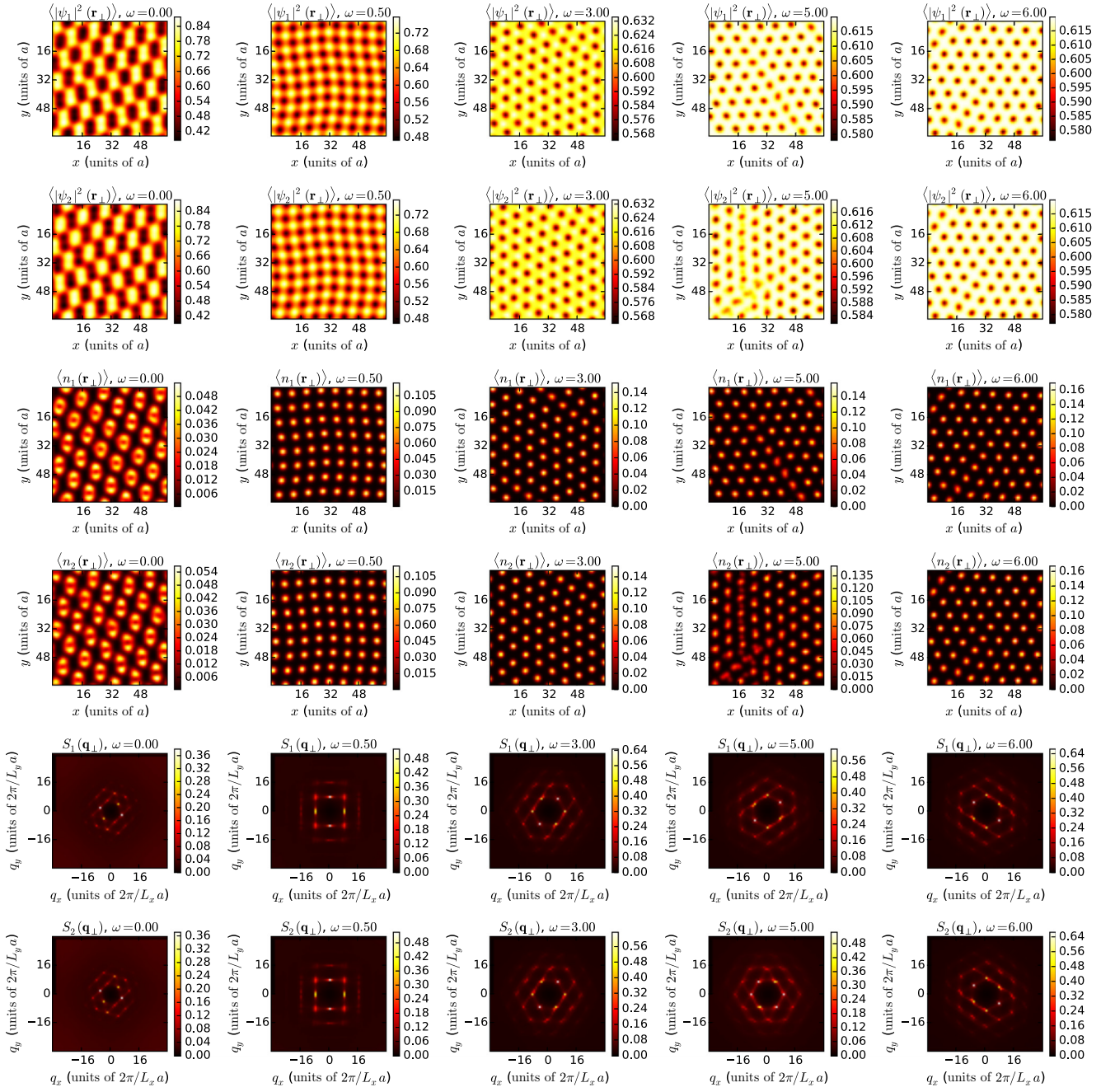

FIG. 11. (Color online) Tableau illustrating the different density and vortex lattices in real space, as the parameter ω increases, i.e., as the intercomponent density-density interaction $2(\eta-\omega)|\psi_1|^2|\psi_2|^2$ decreases. This interaction promotes a square density and vortex lattice. The parameters f, β, and η are fixed to $f=1/64$, $\beta=1.5$, and $\eta=5$ while ω is increased from 0.0 to 6.0 horizontally. The six rows show, from top to bottom the amplitude densities of components 1 and 2, the vortex densities of components 1 and 2, and the structure factors of components 1 and 2. For $\omega=0$, which is the SU(2)-symmetric case, the system exhibits a dimerized phase in component 1, which is complementary to a dimerized phase in component 2, shifted with respect to that of component 1 by an amount corresponding to the lattice constant of the density lattice. The ground state, where the roles of components 1 and 2 are interswitched, is degenerate with the illustrated phase. Note that an area of the system with a high vortex density always corresponds to an area with a low amplitude density. For the SU(2)-symmetric case, U(1) vortices are not topological. When $\omega\neq 0$, the SU(2) symmetry is broken down to U(1) × U(1), and U(1) vortices are topological. The reduction of the interaction $2(\eta-\omega)|\psi_1|^2|\psi_2|^2$ reduces the tendency towards formation of square density and vortex lattices, leading to an eventual reconstruction to a standard hexagonal vortex lattice, and hence a hexagonal density lattice.

$\omega\neq 0$. Again, the full spectrum of amplitude fluctuations is included, using the methods described in Sec. III.

For parameters $(\eta,\omega,f)=(0.5,1.0,1/16)$ and $(\eta,\omega,f)=(2.0,1.0,1/16)$ the lattices are clearly hexagonal and square, respectively. The hexagonal lattice obtained for $\eta=0.5$ and $\omega=1.0$ was found to have a melting transition at $\beta\approx 0.53$. Figure 9(a) shows the specific heat with a δ-function-like anomaly at this temperature. Around this point, we have

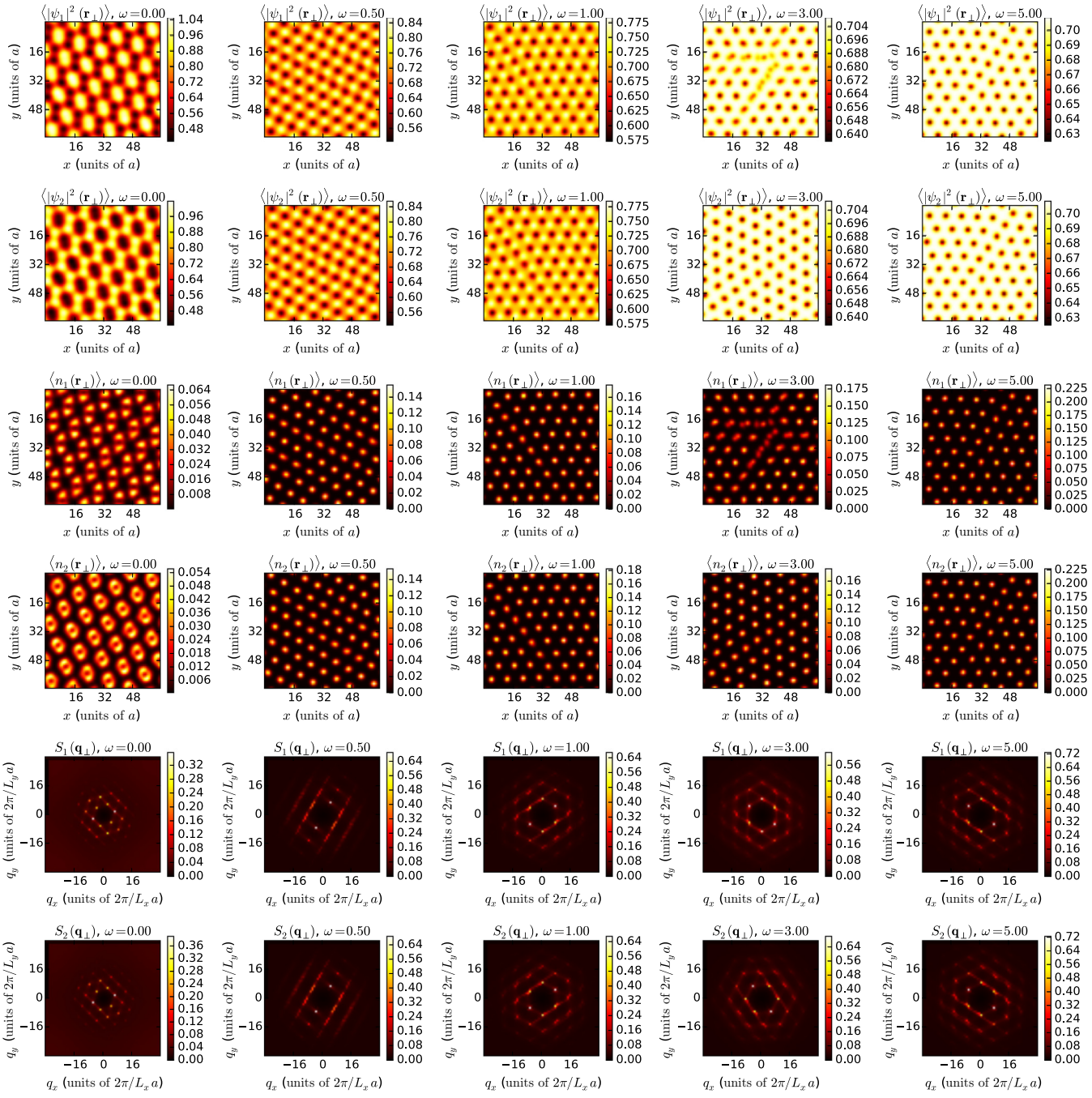

FIG. 12. (Color online) Tableau illustrating the different density and vortex lattices in real space, as the parameter ω increases, i.e., as the intercomponent density-density interaction $2(\eta-\omega)|\psi_1|^2|\psi_2|^2$ decreases. This interaction promotes a square density and vortex lattice. The parameters f, β, and η are fixed to $f = 1/64$, $\beta = 1.5$, and $\eta = 3$ while ω is increased from 0.0 to 5 horizontally. The six rows show, from top to bottom, the amplitude densities of components 1 and 2, the vortex densities of components 1 and 2, and the structure factors of components 1 and 2.

used a closely spaced set of temperatures, in order to get a proper resolution of the anomaly. Figure 9(b) shows the helicity moduli of both components. Both of the z-directed stiffnesses have a zero expectation value in the disordered phase, indicating no phase coherence. In the ordered phase, both of $\langle\Upsilon_{z,i}\rangle$ develop finite expectation values which means that the system has superfluidic properties along the direction of rotation. The two phases are divided by a sharp jump in the longitudinal phase stiffness, a characteristic of a first-order transition. The drop is even sharper than was obtained for the $N = 1$ case, indicating an even larger latent heat associated with the transition. The x- and y-directed stiffnesses remain zero in the ordered state, which rules out any possibility of numerical pinning effects [44,45]. Looking further at the insets of Fig. 9(a), which show the structure factors in the disordered and ordered phases, we see clear evidence of an incoherent vortex liquid at $\beta < 0.53$ in the left inset, while the right inset shows an ordered hexagonal vortex liquid lattice at $\beta > 0.53$.

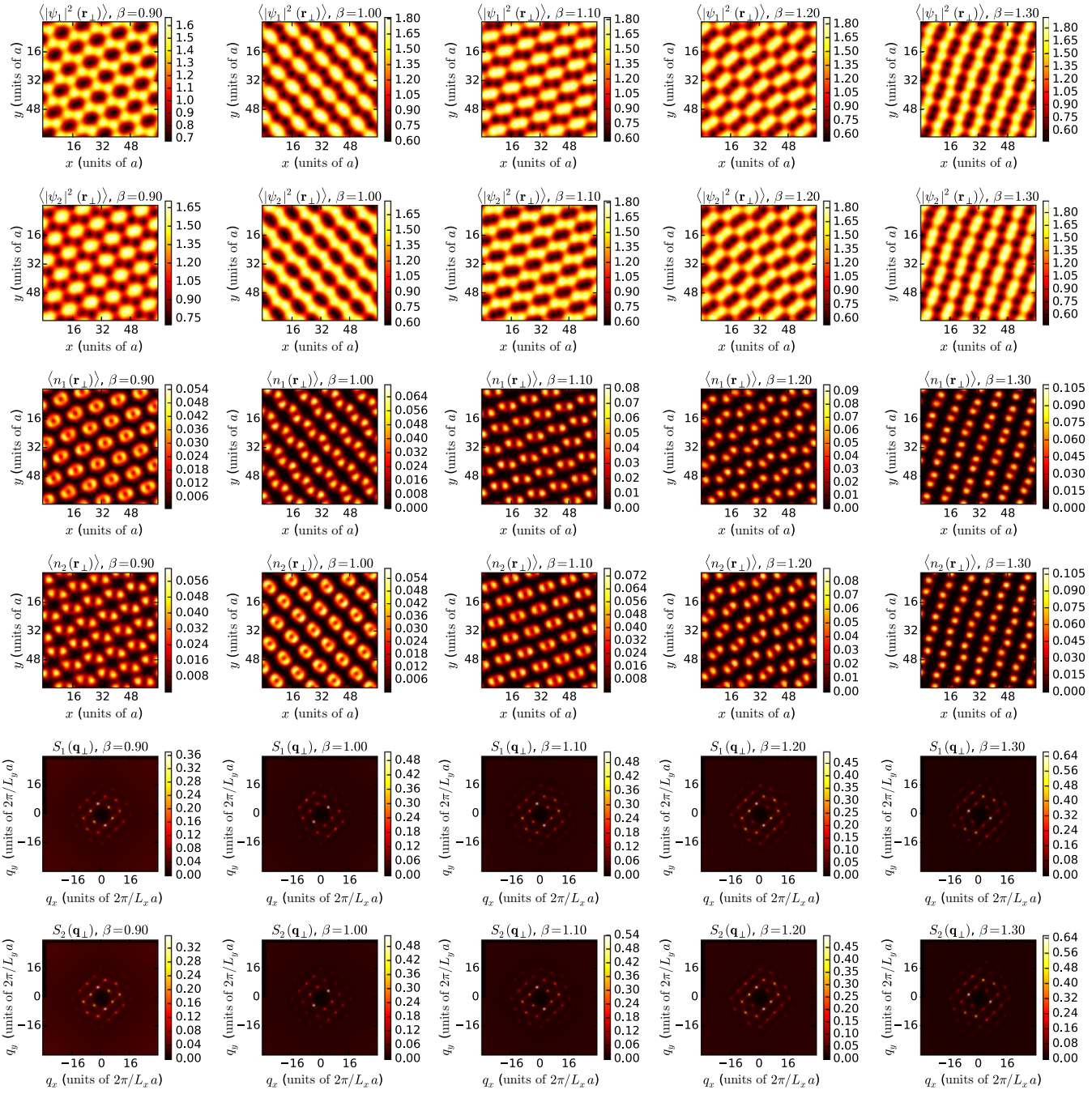

FIG. 13. (Color online) Tableau illustrating the different SU(2) density and vortex lattices in real space, as the parameter β increases. The parameters f, η, and ω are fixed to $f = 1/64$, $\eta = 1.0$, and $\omega = 0.0$ while β is increased from 0.9 to 1.3 horizontally. The six rows show, from top to bottom, the amplitude densities of components 1 and 2, the vortex densities of components 1 and 2, and the structure factors of components 1 and 2. Note how the vortex structures and the density structures always track, that is, an area of the system with a high vortex density always corresponds to an area with a low amplitude density.

Turning to the square lattice, now the parameters in question are $\eta = 2.0$ and $\omega = 1.0$. The transition point is located at $\beta \approx 1.11$. Figure 10(a) shows the specific heat. Again, an anomaly is located at the transition point. The helicity moduli, shown in Fig. 10(b), also show first-order behavior. Both z-directed components are zero on the high-temperature side, and develop a finite value through a sharp jump at the low-temperature side. It is important to also consider the transverse components. Both $\langle \Upsilon_{x,i} \rangle$ and $\langle \Upsilon_{y,i} \rangle$ are zero throughout the area of interest. Here we note that the x-directed modulus drops to a tiny negative value at a point after the transition. This is a nonphysical effect, most likely caused by a metastable state. We believe this is simply a numerical artifact, as we used a lower amount of Monte Carlo time away from the transition. Turning our attention to the structure factors, shown in the insets of Fig. 10(b), we again see the isotropic vortex liquid in

the disordered side of the transition; the ordered side shows a square fourfold symmetry.

Thus, both the square and the hexagonal lattices undergo first-order melting transitions from their respective ordered phases, into an isotropic vortex line liquid.

APPENDIX D: INTERCOMPONENT INTERACTION, AND ITS EFFECT ON DENSITY AND VORTEX LATTICES

In this Appendix, we include more detailed figures of the vortex and density structures in real and reciprocal space, as the intercomponent interaction $2(\eta - \omega)|\psi_1|^2|\psi_2|^2$ is varied, to supplement the points made in Secs. IV A and IV C.

Figures 11 and 12 illustrate how the vortex lattice and the component densities reconstruct as the intercomponent density-density interaction $(\eta - \omega)|\psi_1|^2|\psi_2|^2$ changes. We do this by fixing η at 5.0 and 3.0, respectively, and tuning ω. The inverse temperature β is also fixed in both tableaus. Common in both figures is that the vortices first form two interlaced square lattices for sufficiently small ω, and, by extension, large intercomponent coupling. Then the lattices reconstruct into a hexagonal structure. Note that the hexagonal lattices of the two components start out slightly shifted with respect to each other, but become completely cocentered when $\omega > \eta$. This final state corresponds to an attractive intercomponent coupling.

The behavior of the amplitude densities is explained in Sec. IV A, and we can compare the reasoning to the top two rows of Figs. 11 and 12. First of all, the presence of a vortex locally suppresses the amplitude, which again may affect the immediate neighborhood, depending on the value of the intercomponent coupling. For strong repulsive couplings a suppression of the amplitude of one color in an area leads to an enhancement of the amplitude of the other color in the same area. The absence of vortices in the neighborhood then leads to the opposite effect. This causes staggering of the amplitude densities and formation of distinct vortex sublattices. Considering carefully the range of variation in the amplitudes, it is seen that there are rather large gradients for the square structures. When the coupling is only weakly repulsive or even attractive there is a much less dramatic effect. The variations in the amplitudes are much smaller; there is little to no staggering.

The first column of Figs. 11 and 12 is in a different class from the rest. Here $\omega = 0$, and we are in the SU(2) regime. Figure 13 further illustrates the wide variety of ground states obtainable here. This tableau, in contrast to the two previous ones, has a fixed η and ω, while we vary the inverse temperature β from column to column. These pictures are all taken from a single simulation, evolved through Monte Carlo sampling from a single randomized initial state as β is increased. The vortex lattice initially forms at around $\beta = 0.7$ and evolves continuously. It continues to evolve even at the lowest temperatures ($\beta = 1.5$) used in the simulation. This pattern is common in all simulations done with similar parameter sets.

The common features in the SU(2) lattices are clearly seen in Fig. 13. The vortices tend to form dimers, which usually have some global alignment. The alignment is evident in the Bragg peaks, as we in most cases have two opposing peaks of higher intensity than the rest. The vortex dimer complexes always arrange themselves in a hexagonal structure, which is also seen in the structure factors.

[1] C. J. Myatt, E. A. Burt, R. W. Ghrist, E. A. Cornell, and C. E. Wieman, Phys. Rev. Lett. **78**, 586 (1997).

[2] D. S. Hall, M. R. Matthews, J. R. Ensher, C. E. Wieman, and E. A. Cornell, Phys. Rev. Lett. **81**, 1539 (1998).

[3] M. R. Matthews, B. P. Anderson, P. C. Haljan, D. S. Hall, C. E. Wieman, and E. A. Cornell, Phys. Rev. Lett. **83**, 2498 (1999).

[4] G. Modugno, M. Modugno, F. Riboli, G. Roati, and M. Inguscio, Phys. Rev. Lett. **89**, 190404 (2002).

[5] E. J. Mueller and T.-L. Ho, Phys. Rev. Lett. **88**, 180403 (2002).

[6] K. Kasamatsu, M. Tsubota, and M. Ueda, Phys. Rev. Lett. **91**, 150406 (2003).

[7] V. Schweikhard, I. Coddington, P. Engels, S. Tung, and E. A. Cornell, Phys. Rev. Lett. **93**, 210403 (2004).

[8] S. B. Papp, J. M. Pino, and C. E. Wieman, Phys. Rev. Lett. **101**, 040402 (2008).

[9] G. Thalhammer, G. Barontini, L. De Sarlo, J. Catani, F. Minardi, and M. Inguscio, Phys. Rev. Lett. **100**, 210402 (2008).

[10] K. Kasamatsu and M. Tsubota, Phys. Rev. A **79**, 023606 (2009).

[11] S. Tojo, Y. Taguchi, Y. Masuyama, T. Hayashi, H. Saito, and T. Hirano, Phys. Rev. A **82**, 033609 (2010).

[12] D. J. McCarron, H. W. Cho, D. L. Jenkin, M. P. Köppinger, and S. L. Cornish, Phys. Rev. A **84**, 011603 (2011).

[13] P. Kuopanportti, J. A. M. Huhtamäki, and M. Möttönen, Phys. Rev. A **85**, 043613 (2012).

[14] K. Kasamatsu, H. Takeuchi, M. Tsubota, and M. Nitta, Phys. Rev. A **88**, 013620 (2013).

[15] M. Cipriani and M. Nitta, Phys. Rev. A **88**, 013634 (2013).

[16] Y.-H. Li and S. Teitel, Phys. Rev. Lett. **66**, 3301 (1991).

[17] R. E. Hetzel, A. Sudbø, and D. A. Huse, Phys. Rev. Lett. **69**, 518 (1992).

[18] T. Chen and S. Teitel, Phys. Rev. B **55**, 11766 (1997).

[19] X. Hu, S. Miyashita, and M. Tachiki, Phys. Rev. Lett. **79**, 3498 (1997).

[20] A. K. Nguyen and A. Sudbø, Phys. Rev. B **58**, 2802 (1998).

[21] A. K. Nguyen and A. Sudbø, Phys. Rev. B **57**, 3123 (1998).

[22] S. Ryu and D. Stroud, Phys. Rev. B **57**, 14476 (1998).

[23] A. K. Nguyen and A. Sudbø, Phys. Rev. B **60**, 15307 (1999).

[24] S.-K. Chin, A. K. Nguyen, and A. Sudbø, Phys. Rev. B **59**, 14017 (1999).

[25] A. K. Nguyen and A. Sudbø, Europhys. Lett. **46**, 780 (1999).

[26] H. Nordborg and G. Blatter, Phys. Rev. Lett. **79**, 1925 (1997).

[27] J. Hu and A. H. MacDonald, Phys. Rev. B **56**, 2788 (1997).

[28] M. H. Anderson, J. R. Ensher, M. R. Matthews, C. E. Wieman, and E. A. Cornell, Science **269**, 198 (1995).

[29] K. B. Davis, M.-O. Mewes, M. R. Andrews, N. J. van Druten, D. S. Durfee, D. M. Kurn, and W. Ketterle, Phys. Rev. Lett. **75**, 3969 (1995).
[30] J. R. Abo-Shaeer, C. Raman, J. M. Vogels, and W. Ketterle, Science **292**, 476 (2001).
[31] M. Kobayashi and M. Nitta, J. Low Temp. Phys. **175**, 208 (2014).
[32] H. Feshbach, Ann. Phys. (NY) **19**, 287 (1962).
[33] S. Inouye, M. R. Andrews, J. Stenger, H.-J. Miesner, D. M. Stamper-Kurn, and W. Ketterle, Nature (London) **392**, 151 (1998).
[34] E. K. Dahl, E. Babaev, and A. Sudbø, Phys. Rev. B **78**, 144510 (2008).
[35] E. K. Dahl, E. Babaev, and A. Sudbø, Phys. Rev. Lett. **101**, 255301 (2008).
[36] E. K. Dahl, E. Babaev, S. Kragset, and A. Sudbø, Phys. Rev. B **77**, 144519 (2008).
[37] A. Kuklov, N. Prokof'ev, and B. Svistunov, Phys. Rev. Lett. **92**, 030403 (2004).
[38] A. Kuklov, N. Prokof'ev, and B. Svistunov, Phys. Rev. Lett. **93**, 230402 (2004).
[39] J. Smiseth, E. Smørgrav, E. Babaev, and A. Sudbø, Phys. Rev. B **71**, 214509 (2005).
[40] E. V. Herland, E. Babaev, and A. Sudbø, Phys. Rev. B **82**, 134511 (2010).
[41] E. Babaev, L. D. Faddeev, and A. J. Niemi, Phys. Rev. B **65**, 100512 (2002).
[42] J. Garaud, J. Carlström, E. Babaev, and M. Speight, Phys. Rev. B **87**, 014507 (2013).
[43] M. E. Fisher, M. N. Barber, and D. Jasnow, Phys. Rev. A **8**, 1111 (1973).
[44] M. Franz and S. Teitel, Phys. Rev. Lett. **73**, 480 (1994).
[45] S. Hattel and J. Wheatley, Phys. Rev. B **50**, 16590 (1994).
[46] N. Metropolis, A. W. Rosenbluth, M. N. Rosenbluth, A. H. Teller, and E. Teller, J. Chem. Phys. **21**, 1087 (1953).
[47] W. K. Hastings, Biometrika **57**, 97 (1970).
[48] S. B. Chung and S. A. Kivelson, Phys. Rev. B **82**, 214512 (2010).
[49] K. M. Mertes, J. W. Merrill, R. Carretero-González, D. J. Frantzeskakis, P. G. Kevrekidis, and D. S. Hall, Phys. Rev. Lett. **99**, 190402 (2007).
[50] G. Thalhammer, M. Theis, K. Winkler, R. Grimm, and J. H. Denschlag, Phys. Rev. A **71**, 033403 (2005).
[51] T. Volz, S. Dürr, S. Ernst, A. Marte, and G. Rempe, Phys. Rev. A **68**, 010702 (2003).
[52] D. V. Freilich, D. M. Bianchi, A. M. Kaufman, T. K. Langin, and D. S. Hall, Science **329**, 1182 (2010.
[53] M. A. Cazalilla and A. M. Rey, Rep. Prog. Phys. **77**, 124401 (2014).
[54] A. V. Gorshkov, M. Hermele, V. Gurarie, C. Xu, P. S. Julienne, J. Ye, P. Zoller, E. Demler, M. D. Lukin, and A. M. Rey, Nat. Phys. **6**, 289 (2010).
[55] S. Kragset, E. Babaev, and A. Sudbø, Phys. Rev. Lett. **97**, 170403 (2006).
[56] S. Kragset, E. Babaev, and A. Sudbø, Phys. Rev. A **77**, 043605 (2008).
[57] J. Carlström, E. Babaev, and M. Speight, Phys. Rev. B **83**, 174509 (2011).
[58] D. F. Agterberg, E. Babaev, and J. Garaud, Phys. Rev. B **90**, 064509 (2014).